

RESEARCH ARTICLE | MAY 24 2024

Temperature effects on the nanoscale thermoelastic response of a SiO₂ membrane

Special Collection: [Open Framework Materials](#)


Danny Fainozzi  ; Federico Caporaletti  ; Flavio Capotondi; Dario De Angelis  ; Ryan A. Duncan; Laura Foglia  ; Alessandro Martinelli  ; Riccardo Mincigrucci  ; Keith A. Nelson  ; Emanuele Pedersoli  ; Marco Zanatta  ; Alexei A. Maznev; Giulio Monaco; Filippo Bencivenga  ; Giacomo Baldi  



APL Mater. 12, 051122 (2024)
<https://doi.org/10.1063/5.0201769>



APL Materials
Special Topic: 2D Materials
for Biomedical Applications
Submit Today



Temperature effects on the nanoscale thermoelastic response of a SiO₂ membrane

Cite as: APL Mater. 12, 051122 (2024); doi: 10.1063/5.0201769

Submitted: 31 January 2024 • Accepted: 23 April 2024 •

Published Online: 24 May 2024



View Online



Export Citation



CrossMark

Danny Fainozzi,^{1,a)} Federico Caporaletti,² Flavio Capotondi,¹ Dario De Angelis,³ Ryan A. Duncan,⁴ Laura Foglia,¹ Alessandro Martinelli,⁵ Riccardo Mincigrucci,¹ Keith A. Nelson,⁴ Emanuele Pedersoli,¹ Marco Zanatta,⁶ Alexei A. Maznev,⁴ Giulio Monaco,⁷ Filippo Bencivenga,^{1,b)} and Giacomo Baldi^{6,c)}

AFFILIATIONS

¹ Elettra - Sincrotrone Trieste S.C.p.A., Basovizza, 34149 Trieste, Italy

² Laboratory of Polymer and Soft Matter Dynamics, Experimental Soft Matter and Thermal Physics (EST), Université Libre de Bruxelles (ULB), Brussels 1050, Belgium

³ CNR-IOM, AREA Science Park, Basovizza, 34149 Trieste, Italy

⁴ Department of Chemistry, Massachusetts Institute of Technology, Cambridge, Massachusetts 02139, USA

⁵ Laboratoire Charles Coulomb, Université de Montpellier, CNRS, 34095 Montpellier, France

⁶ Department of Physics, Università di Trento, 38123 Trento, Italy

⁷ Department of Physics and Astronomy, Università di Padova, 35131 Padova, Italy

Note: This paper is part of the Special Topic on Open Framework Materials.

^{a)} danny.fainozzi@elettra.eu

^{b)} filippo.bencivenga@elettra.eu

^{c)} **Author to whom correspondence should be addressed:** giacomo.baldi@unitn.it

ABSTRACT

We crossed two femtosecond extreme ultraviolet (EUV) pulses on a 100 nm thick amorphous membrane of SiO₂, generating transient gratings (TGs) of light intensity with 84 nm spatial periodicity. The EUV TG excitation gave rise to the efficient generation of Lamb waves (LWs) and of a temperature grating, whose dynamics was studied at two different initial sample temperatures, 50 and 300 K. The short penetration depth of the EUV excitation pulses turned into a strong non-uniformity in the actual temperature as a function of the depth from the sample surface. At the lowest temperature, the LW frequencies presented a sizable shift in time due to the thermal equilibration along the membrane thickness. The analysis of the EUV TG waveforms allowed us to determine the decay time of the thermal grating and the sound attenuation coefficient, both found in reasonable agreement with the literature. The results show how EUV TG can provide information of non-equilibrium thermoelastic dynamics in thin membranes transparent to optical radiation.

© 2024 Author(s). All article content, except where otherwise noted, is licensed under a Creative Commons Attribution-NonCommercial-NoDeriv 4.0 International (CC BY-NC-ND) license (<https://creativecommons.org/licenses/by-nc-nd/4.0/>). <https://doi.org/10.1063/5.0201769>

I. INTRODUCTION

Studying the thermal properties and the vibrational dynamics of materials with typical spatial dimensions of a few tens of nanometers is critical for advancing their technological application. The development of faster, more efficient, and more compact nanoelectronic devices, such as smartphones and computer chips,

as well as improved thermal barrier coatings,¹ heat-assisted magnetic recording,² nano-enhanced photovoltaics, and thermoelectric energy conversion devices, could significantly benefit from a better understanding of the basic mechanisms governing nanoscale thermal transport. These devices often involve structured thin films composed of layers of different chemical composition, with impurities added to tailor their functionality.³ However, the complex

structure of these materials makes it challenging to predict and characterize their thermoelastic properties.

Material properties, such as elasticity, thermal conductivity, and heat capacity, can drastically differ when the spatial dimensions reduce from macroscopic to sub- μm scales,⁴ i.e., to sizes comparable with the characteristic length scales of thin membranes and other nanostructures. Over the years, an obstacle to fully describing thermoelastic responses of such thin samples has been the absence of experimental techniques capable of accessing the tens of nanometer length scale range⁵ without the requirement of modifying or touching the sample. In addition, contactless probes like optical spectroscopy often rely on the need for samples with either a tangible absorption of radiation or a significant scattering volume, thus making it difficult to study samples that are simultaneously optically transparent and with thicknesses in the sub- μm range. The emergence of free electron laser (FEL) sources has provided opportunities to exploit extreme ultraviolet (EUV) pulses to extend the transient grating (TG) approach to shorter wavelengths, down to a few tens of nanometers, overcoming the aforementioned issue of optical transparency in thin membranes, since all materials are strongly absorbing at EUV wavelengths. This advancement enabled investigations of nanoscale thermoelasticity in sub- μm membranes and in a contact-less fashion.^{6–9} The development of experimental methods to probe the sound attenuation in thin films and membranes in a wide frequency range is of great relevance for various applications. We can mention, for instance, the need to better understand the mechanisms responsible for thermal noise in gravitational wave interferometers. Thermal noise originates from relaxation processes active in the mirror coatings, composed of multilayers of amorphous films, where the signal layer has a thickness of about 100 nm.^{10,11}

The investigation of the sound propagation and damping in amorphous solids in the frequency interval between 100 GHz and 1 THz poses a significant experimental challenge also for bulk samples.^{12–21} Brillouin light scattering (BLS) is typically limited to acoustic frequencies of tens of gigahertz,²² while inelastic x-ray scattering (IXS) is confined to frequencies above one terahertz.^{16,17} Brillouin ultraviolet light scattering has allowed us to extend the BLS range up to ≈ 100 GHz,^{13–15,23} while picosecond ultrasonic techniques (PUTs) are being used in recent years to probe frequencies extending up to the terahertz range.^{18–21} Brillouin scattering methods, with both light and x-ray radiation, can be used on bulk samples, while PUTs are applicable only on thin films, deposited on the appropriate substrate. PUTs are pump-probe experiments, where an hypersonic pulse is launched by the pump and its echoes at the film interface are detected by the probe beam. The method usually requires the deposition of thin metallic films, which act as transducers, on the material under study and the use of different sample thicknesses to determine the sound attenuation coefficient.¹⁸

Here, we exploit EUV TG to probe the thermoelastic response of a freestanding membrane of amorphous SiO_2 , with a thickness of 100 nm, at two different initial temperatures, $T_i = 50$ K and $T_i = 300$ K. Our method does not require the presence of a substrate or the deposition of a transducer and allows us to measure the time dependence of the waveform, including the decay of the thermal grating and the propagation and attenuation of sound in the membrane. Here, we report the measurement of the waveforms at the two probed temperatures for a specific value of the grating wavevector, $q = 0.075 \text{ nm}^{-1}$. The method can also be used at higher

wavevectors, to cover a broad frequency range between 50 and 500 GHz.

II. METHODS

TG is a third-order non-linear optical technique (a four-wave-mixing process), wherein two pulses of equal wavelength λ (referred to as pumps) are temporally and spatially overlapped on the sample at a crossing angle of 2θ . Assuming parallel polarization of the beams, the interference between these two pulses induces a spatial modulation in light intensity, which exhibits a periodicity $\Lambda_{\text{TG}} = \lambda / (2 \sin \theta)$; refer to Fig. 1(a) for a visual representation. The resulting spatially periodic material excitation acts as a transient diffraction grating for a third variably delayed pulse (probe), with wavelength λ_{pr} , giving rise to a fourth pulse: the diffracted beam (signal); see Fig. 1(b).

The experiment was performed at the TIMER beamline at the FERMI FEL in Trieste, Italy. The instrument is described in detail elsewhere.²⁴ Two time-coincident ≈ 50 fs full width at half maximum (FWHM) EUV pulses were intersected on the surface of an amorphous SiO_2 membrane (thickness $d = 100$ nm) at the angle $2\theta = 27.6^\circ$ (set with 2% accuracy), generating a TG, whose wavevector is aligned along the sample's surface. The pump wavelength, λ , was set to 39.9 nm, resulting in a grating period of $\Lambda_{\text{TG}} \approx 84$ nm.

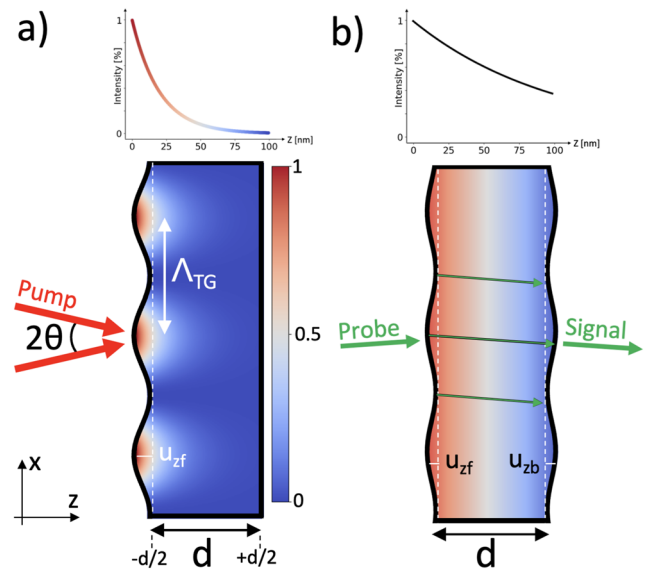


FIG. 1. (a) Schematic configuration of the EUV TG excitation. Two pump beams, having the same wavelength λ , are overlapped in space and time on the sample at a crossing angle of 2θ , resulting in an intensity grating with modulation parallel to the surface. This spatially periodic excitation, with a period Λ_{TG} , results in an initial thermal gradient given by the sample's absorption (as visible in the graph on top), causing thermal expansion that generates acoustic modes generally referred to as Lamb waves (LWs), propagating in the (x, z) -plane; the reference frame is in the bottom-left corner. Panel (b) illustrates the sample after the pump pulse is passed. Heat propagates along z reaching the opposite end of the sample in ≈ 5 ns (see Sec. IV B for a detailed estimate). The thermoelastic response driven by the EUV TG is probed by a third pulse, the probe, and detected in a forward diffraction geometry. The graphs on top of panels (a) and (b) illustrate, respectively, the absorption of pump and probe pulses along z .

The probe pulse (≈ 50 fs FWHM, $\lambda_{pr} = 13.3$ nm) impinged on the sample with an angle of 4.6° with respect to the surface normal. The forward-diffracted signal was detected in transmission using a CCD camera, following the methodology outlined in Refs. 6 and 25. The sample was kept in thermal contact with the cold finger of a He cryostat in order to vary its initial temperature (T_i), i.e., the temperature before the arrival of the FEL pump; the measurements were carried out at $T_i = 50$ and 300 K.

The SiO₂ membranes were purchased from SiMPore, Inc. The membrane layer is deposited via plasma enhanced chemical vapor deposition (PECVD) using TEOS as a source material. A thin film of SiO₂ is first deposited on a Si substrate. Afterward, the substrate is etched from below, to leave a surface of 1×1 mm² of free membrane, as described in Ref. 26. The membrane thickness is guaranteed by the manufacturer to be $d = 100$ nm \pm 10%. Ellipsometry shows a refractive index very similar to that of bulk silica, indicating a similar mass density. The elastic properties of films of SiO₂ prepared with the same deposition method but of higher thickness have been measured by BLS.²⁷

III. RESULTS

The EUV excitation pulses are strongly absorbed by the sample, the absorption length L_{abs} being 20 nm, as displayed by the top curve in Fig. 1(a). This leads to a strong thermal gradient along the sample depth, in addition to the generation of the thermal grating, which, via thermal expansion, turns into a density grating and in a spatially periodic surface displacement of the front surface (U_{zf}), of the order of a few pm (largely exaggerated in Fig. 1).²⁸ The impulsive excitation gradient ($L_{abs} < d$) induced by the EUV pump launches a spectrally broad acoustic wavepacket propagating across the sample and reaching its back-side, after a time that depends on material longitudinal sound velocity and layer thickness. At the same time, the heat propagates from the front to the back side of the sample until an average temperature is reached. While such relaxations occur, one should expect that the amplitude of the displacement of the back surface (U_{zb}) progressively becomes comparable to U_{zf} ; see Fig. 1(b).

Note that while the acoustic perturbation reaches the opposite side of the membrane in a time frame $\approx v/d \approx 17$ ps, considering a sound speed $v \sim 6000$ m/s, heat propagates much slower, reaching the opposite end of the sample in ≈ 5 ns, a value that can be determined directly from the decay of the measured waveform. We postpone this estimate to Sec. IV B, where we will also compare the grating thermal decay time with the macroscopic thermal diffusivity. The longer absorption length of the probe pulse in the sample [~ 100 nm; see the upper curve in Fig. 1(b)] and the slow heat propagation make it, in principle, possible to follow the heat transfer throughout the sample during the hundred of picoseconds timescale characteristic of the EUV TG signal. As we are going to show in Sec. III A, this thermal dynamics is appreciable when $T_i = 50$ K, since here the heat capacity is lower, and the average temperature rise given by the TG excitation and the relative temperature change induced are larger.

The red lines in Figs. 2(a) and 2(b) are the EUV TG signal as a function of the relative time delay (Δt) between the EUV TG excitation and the probe pulse, collected at $T_i = 300$ and 50 K, respectively. The two waveforms are primarily characterized by a slow decay,

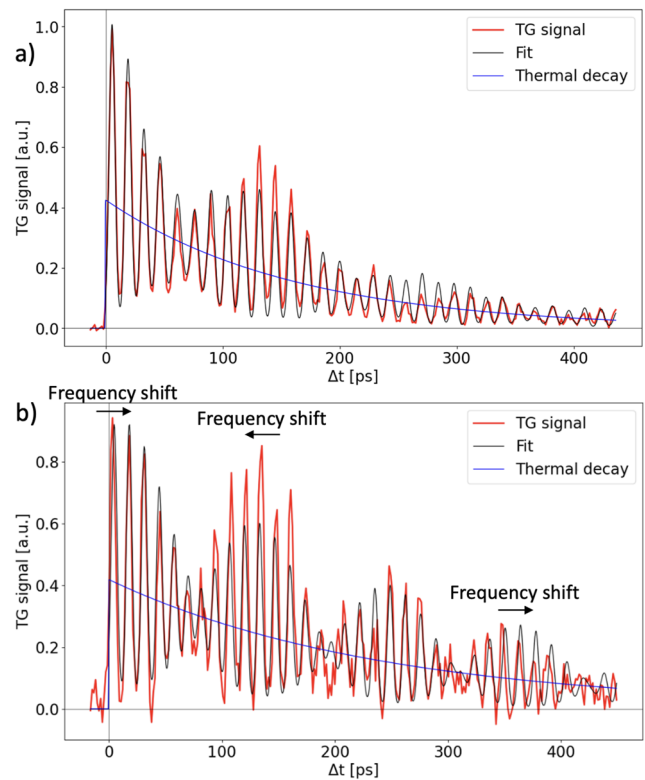


FIG. 2. Panel (a) shows the EUV-TG data (in red) obtained at $T_i = 300$ K. The blue and black lines represent the best fits obtained by using Eqs. (1) and (2), respectively. Panel (b) shows the same for $T_i = 50$ K. Here, frequency shifts (indicated by the arrows) are visible. The trace at 50 K presents a higher noise (visible at $\Delta t < 0$), resulting in a poorer accuracy in the extraction of the acoustic and thermal decay constants from the fit.

which can be attributed to the thermal relaxation of the EUV TG, modulated by acoustic oscillations.^{6,28} The presence of a beating indicates the excitation of waveguide acoustic modes with similar frequencies. Furthermore, while the thermal relaxation has a comparable timescale for the two values of T_i , the beating pattern is evidently more damped at $T_i = 300$ K; this evidence from the raw data indicates that the damping of acoustic modes tangibly depends on T_i .

A. Data analysis

The presence of multiple acoustic modes in TG experiments is expected when d is comparable or shorter than Λ_{TG} . In such a case, the TG launches acoustic modes known as Lamb waves (LWs), which propagate in the (x, z)-plane [the reference frame is shown in Fig. 1(a)] guided by the boundaries of the medium.^{9,29–31} Among the several LWs that can be launched, the one providing the more sizable response in TG experiments are the symmetric modes that more strongly change the experimental observable, which for an EUV probe pulse are primarily the modulations of the density and of the surface displacement (or sample thickness), with the latter typically weaker when the EUV TG signal is detected in transmission,

as in the present case.²⁵ Such modes are those having frequencies (or velocities) closer to the ones of longitudinal acoustic (LA) modes, i.e., density modulations propagating in the bulk of the membrane, and surface acoustic wave (SAW), i.e., a coherent surface displacement propagating at the surface of the membrane. In the present case, the LWs that mostly contribute to the experimental signal are denoted as LW_{S0}, whose nature is closer to the SAW, and LW_{S1} and LW_{S2}, whose nature is closer to that of the LA mode. This is immediately visible by converting the measured frequencies (ν_{LW}) to sound velocities c_{LW} using the formula $c_{LW} = \Lambda_{TG} \cdot \nu_{LW}$, providing a LW_{S0} sound velocity similar to the SAW velocity (c_{SAW}) and

a LW_{S1} sound velocity similar to the LA mode velocity (c_{LA}).^{15,32–35} LW_{S1} and LW_{S2}, since they are closer in frequency, are responsible for the prominent beating evident in the raw data; see Fig. 2.

To provide a quantitative description of the experimental waveforms, an initial fitting procedure was conducted by using the following equation:³⁶

$$I(t) = \left| \frac{1}{2} \left[1 + \operatorname{erf} \left(\frac{\Delta t}{\sigma} \right) \right] \cdot A e^{-\frac{\Delta t}{\tau}} \right|^2, \quad (1)$$

where the *erf* function accounts for the sudden rise of the signal (with σ representing the width of the rise), which is followed by an exponential (thermal) decay of the grating characterized by a time constant τ and amplitude A . The fitting results are reported as blue lines in Fig. 2. Subsequently, Fourier transforms (FTs) were computed on the differences between the measured traces and their respective exponential fits (hereafter referred to as residual), to identify the main acoustic frequencies. The analysis is described in detail below and indicates that the acoustic modes are dominated by two LWs. Consequently, the complete fitting procedure of the waveforms in the time domain, shown as the black line in

TABLE I. Time decays and frequencies obtained from the fitting procedure using Eq. (2). The larger error associated with the trace at $T_i = 50$ K is due to the trace's lower signal-to-noise ratio.

T_i (K)	τ (ps)	τ_S (ps)	ν_{S1} (GHz)	ν_{S2} (GHz)
50	470 ± 110	510 ± 120	70.37 ± 0.12	78.03 ± 0.09
300	328 ± 49	275 ± 25	71.87 ± 0.05	78.36 ± 0.13

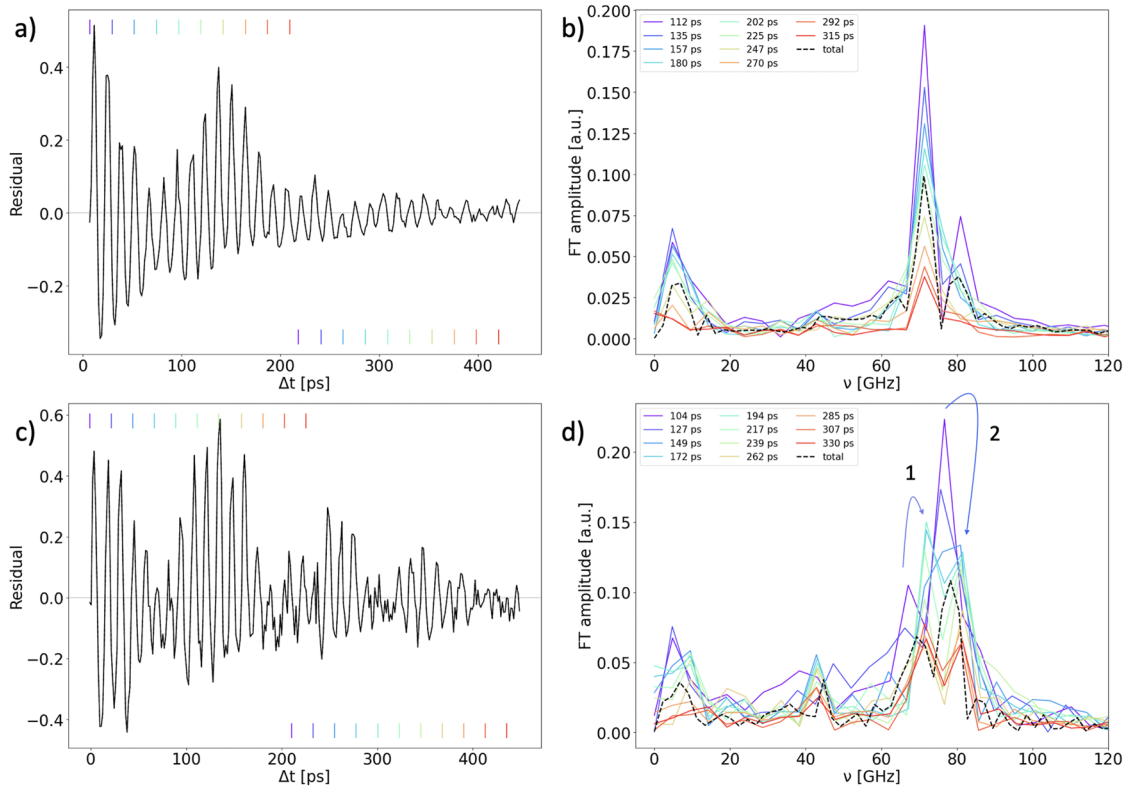


FIG. 3. Panel (a) and (c) display the residuals, i.e., the difference between the TG signal and the best fit with Eq. (1), at $T_i = 300$ K and $T_i = 50$ K, respectively. The color bands on top and bottom illustrate, respectively, the initial and final points of the trace considered to perform the sequence of FTs (wavelets), which are displayed in (b) and (d). The FTs have been performed over Δt windows of 210 ps, whose central values are displayed in the legend. The full residual FT is displayed as the black dashed line for completeness. The wavelets in (b) show constant frequencies throughout the measurement. Meanwhile, at $T_i = 50$ K [panel (d)], we see pronounced frequency shifts (i.e., exceeding the FWHM of the peaks), which are labeled by the numbered arrows and are interpreted as signatures of temperature variations occurring during the measurement.

Figs. 2(a) and 2(b), incorporates two additional damped sinusoidal terms (with the same decay constant τ_S) into Eq. (1), i.e., the LW_{S1} and the LW_{S2} ,

$$I(t) = \left[\frac{1}{2} \left[1 + \operatorname{erf} \left(\frac{\Delta t}{\sigma} \right) \right] \cdot \left[A e^{-\frac{\Delta t}{\tau}} + A_{S1} \sin(2\pi \nu_{S1} \Delta t + \phi_{S1}) e^{-\frac{\Delta t}{\tau_S}} + A_{S2} \sin(2\pi \nu_{S2} \Delta t + \phi_{S2}) e^{-\frac{\Delta t}{\tau_S}} \right] \right]^2, \quad (2)$$

returning the parameters in Table I.

As can be seen in Fig. 2(a), the fit employing two frequencies matches well the data at $T_i = 300$ K, while for $T_i = 50$ K, a small frequency shift appears toward the tail of the signal in Fig. 2(b). The latter can be associated with the variation in the temperature distribution inside the sample during the measurement, due to heat propagation. This is appreciable at $T_i = 50$ K, given the lower heat capacity and higher temperature rise of the sample with respect to $T_i = 300$ K.

To further understand this behavior, we performed a set of Fourier Transforms (FTs) on the difference between the TG signal and its thermal decay, which we call the “residual,” by taking into consideration different windows in Δt , with the same width but different central values. Figure 3(a) shows the residual at $T_i = 300$ K and the employed Δt -windows. The color bands on top and bottom of this figure show, respectively, the initial and final points of the trace considered to perform the sequence of FTs that are computed with a fixed $\Delta t = 210$ ps and progressively increasing the central time, whose value is indicated in the legend of Fig. 3(b). The FT of the full residual is also displayed as the black dashed line. The most prominent features of the FTs are the two modes, LW_{S1} at ≈ 70 GHz and LW_{S2} at ≈ 80 GHz. The peak at ~ 10 GHz is the frequency difference between the two, which is present due to the quadratic nature of the TG signal [see Eq. (2)]. At this temperature, the frequency content in the associated FT does not substantially change (each mode’s frequency is within its FWHM), as shown in Fig. 3(b). This is an indication that the beam-induced temperature increase at room temperature is such that the elastic properties of the material do not change appreciably compared to the FTs’ frequency resolution.

On the contrary, the same analysis on the residual at $T_i = 50$ K Fig. 3(c) shows substantial frequency shifts, highlighted by arrows 1 and 2 in Fig. 3(d), respectively, for the LW_{S1} and LW_{S2} modes. Given the slow ≈ 5 ns timescale for heat transport across the sample’s thickness (see Sec. IV B for more details), the temperature distribution across the membrane is highly inhomogeneous, with the front surface at an average temperature, \bar{T} , significantly higher than that of the back surface, which remains close to T_i for the entire time window of the measurement.

Two other weaker peaks can be spotted in the FTs, associated with two additional modes, LW_{S0} at ≈ 43 GHz and LW_{A1} at ≈ 63 GHz. The signal associated with LW_{S0} mainly comes from symmetric surface displacements. The antisymmetric mode LW_{A1} can be spotted in Fig. 3(b) and in a few FTs also in Fig. 3(d). This mode is expected to produce a lower signal because we are most sensitive to the density variations and the average density change along the membrane thickness is zero for antisymmetric modes.

B. Estimate of the average sample temperature

To consolidate this argument, following Ref. 8, we estimate the average temperature rise ΔT of the sample given the energy density deposited by the pumps,

$$\Delta T \approx \frac{F}{\rho \bar{d}} \frac{1}{\bar{C}(\Delta T)}, \quad (3)$$

where F is the fluence of the pumps, ρ is the density of the sample, \bar{d} is the interaction length within the sample, and $\bar{C}(\Delta T)$ is the integral of the heat capacity (C) over ΔT , i.e.,

TABLE II. Minimum, maximum, and average estimated temperature rise of the membrane obtained using Eqs. (3) and (4). The LW_{S1} frequency has also been used to extrapolate the final temperature of the sample.

T_i (K)	ΔT_{\min} (K)	ΔT_{\max} (K)	$\Delta T_{(\min+\max)/2}$ (K)	LW_{S1} (K)
50	≈ 80	≈ 150	≈ 115	≈ 105
300	≈ 30	≈ 65	≈ 47.5	≈ 60

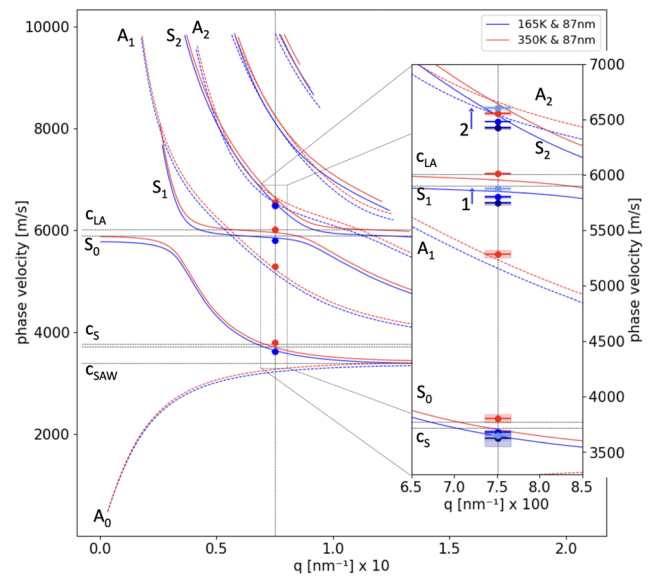


FIG. 4. LW dispersion curves calculated for the estimated values of $\bar{T} = T_i + \Delta T_{(\min+\max)/2}$ (blue and red lines) and a thickness of 87 nm. The solid and dashed lines represent the symmetric and antisymmetric modes, respectively. The values of c_S and c_{LA} are also plotted for the two temperatures. The red dots show the frequencies of the modes at $T_i = 300$ K as obtained from the fit (LW_{S1} and LW_{S2} branches) and from the FTs (LW_{S0} and LW_{A1} branches). The blue dots are the same frequencies at $T_i = 50$ K, as obtained by fitting the data in a Δt window of 210 ps and shifting this window along the Δt axis (wavelet analysis). The results corresponding to the initial portion, middle portion, and last portion of the waveform are reported as dark blue, blue, and light blue, respectively. The trends of these frequencies, labeled with numbers from 1 to 4, match the behavior expected from the wavelet analysis of the FTs shown in Fig. 3(d). The error bars in q represent the error associated with the incidence angle of the probe (set with 2% accuracy), while the error bars in the phase velocity represent the error from the fit (S_1 and S_2) or the FTs (S_0 and A_1).

29 May 2024 13:29:00

$$\bar{C}(\Delta T) = \frac{1}{\Delta T} \int_{T_i}^{T_i + \Delta T} C(T) dT. \quad (4)$$

We estimated the extremes of the temperature rise by considering two different interaction lengths, i.e., $\bar{d} = d$ and $\bar{d} = L_{\text{abs}}/(1 - 1/e)$. The latter considers only the fraction of pump energy deposited in one absorption length; it is representative of the initial excitation conditions [see also Fig. 1(a)] and corresponds to the larger temperature rise (ΔT_{max}). The former assumes that all the pump energy is released in the full thickness of the sample and corresponds to the minimum temperature rise ΔT_{min} . The results of these estimates are illustrated in Table II. The average between these two estimates, $\Delta T_{(\text{min}+\text{max})/2}$, is in quite good agreement with the sound velocity values retrieved using the frequency of the LW_{S1} , which is expected to be closer to the LA velocity (c_{LA}) as discussed in Sec. IV and illustrated in Fig. 4. These different values confirm a much more pronounced temperature rise at $T_i = 50$ K, which permitted us to appreciate effects due to time-dependent changes in the temperature distribution, occurring during the measurement. However, we note that the value of ΔT_{min} is likely more relevant for LWs, whose strain pattern is distributed over the entire membrane thickness, while ΔT_{max} is probably more appropriate for the thermal grating; a more accurate description would imply to account for the time and spatial dependence of the temperature rather than considering average values.

IV. DISCUSSION

A. Lamb wave dispersion

Lamb waves are solutions to the wave equation, derived for a solid plate having an infinite extent in the x and y directions and a finite one in the z direction (corresponding to the membrane thickness d). The physical boundary condition for the free surfaces of the plate is that the component of stress in the z direction at $z = \pm d/2$ is zero. Applying these two conditions to the sinusoidal solutions to the wave equation, a pair of characteristic equations can be found.^{9,29–31} The solutions of these equations lead to the definition of symmetric and antisymmetric modes, meaning that these solutions are a family of waves whose motion is symmetrical/antisymmetrical about the midplane of the plate ($z = 0$).

We performed calculations of the LW dispersion for different temperatures and thicknesses of the SiO_2 membrane. The values of c_{LA} and the shear sound velocity (c_s) were retrieved from Refs. 15 and 35 and interpolated at the desired temperature. The sound velocity of the surface acoustic wave (c_{SAW}) measured independently on a bulk sample of SiO_2 in reflection mode is in good agreement with the one calculated from those literature values.⁸ The results are shown in Fig. 4 for $d = 87$ nm, a value that provides a good agreement of the calculated LW dispersion curves with the experimental frequencies and is in reasonable agreement with the range (100 ± 10 nm) provided by the manufacturer. Here, the red and blue lines represent the LW dispersion at 350 and 165 K, respectively, i.e., the estimated value of $T_i + \Delta T_{(\text{min}+\text{max})/2}$, as reported in Table II. The solid lines illustrate the symmetric modes, and the dashed lines represent the antisymmetric modes.

The red dots are the frequencies of the modes retrieved from the fitting procedure using Eq. (2) for the LW_{S1} and LW_{S2} modes and from the FT for the LW_{S0} and LW_{A1} modes. The blue dots represent

the frequencies obtained using Eq. (2) on a 210 ps window of the trace, i.e., the initial window has been used for the dark blue color; the results from the central region of the spectrum are in blue and the results from the last part are in light blue. We find a qualitative agreement between the calculated dispersions and the results of the wavelet analysis [see Fig. 3(d)], although the weakness of the LW_{S0} and LW_{A1} features prevents us from making a conclusive statement for such modes.

B. Decay of the thermal grating

The decay rate of the thermal grating, quantified by the parameter τ in Eq. (2), can be compared to the values expected from measurements of the thermal diffusivity, $D_{\text{th}} = k_T/(\rho c_v)$, where k_T is the thermal conductivity, ρ is the mass density, and c_v is the specific heat. The value of τ depends on the wavevector of the thermal grating, $q = 2\pi/\Lambda_{\text{TG}} = 0.075 \text{ nm}^{-1}$ in the present case. Assuming the validity of the Fourier law of heat conduction and D_{th} as a constant in time and space all over the sample, the process of thermal diffusion in the direction of the grating at a given q follows the thermal decay time:³⁷

$$\tau(q) = \frac{1}{D_{\text{th}} q^2}. \quad (5)$$

The thermal decay times derived from our TG experiment are compared to the values of the thermal diffusivity from the literature in Fig. 5(a).

The thermal conductivity is known to depend on d for thicknesses below ~ 100 nm.³⁸ This trend is normally explained in terms of a small thermal resistance associated with the interface between the film and the substrate, an interface that is absent in our case since we used a freestanding membrane.³⁸ The thermal decay for our measurement with $T_i = 300$ K is in good agreement with the value of thermal conductivity for the film of 92 nm thickness, in a sample of PECVD silica, the same method used in the fabrication of the present membranes. It is worth noting that the bulk value of the thermal conductivity of $v\text{-SiO}_2$ depends quite strongly on the specific sample, and one can find values that differ by as much as 50% in the literature.^{39,40}

The thermal decay we measure in the sample with $T_i = 50$ K is, in contrast, approximately two times longer than the value expected from the comparison with the diffusivity at the estimated sample temperature, \bar{T} . The main difference between the two measured temperatures is in the relative temperature change induced by the FEL pump beam. Using the mean temperature rise estimated in Table II, we find that at $T_i = 50$ K, there is a $\Delta T/T_i \sim 200\%$, while at $T_i = 300$ K, we have $\Delta T/T_i \sim 15\%$. As a consequence, the sample at $T_i = 50$ K experiences a temperature distribution with a strong inhomogeneity over lengths of tens of nanometers, a fraction of Λ_{TG} . The observed discrepancy is most probably related to the strong temperature inhomogeneity caused by the TG excitation, possibly because the definition of an average thermal diffusivity is not appropriate for such an out-of-equilibrium situation.

Let us now discuss the thermal diffusion across the membrane thickness. The FEL pump pulses generate a sudden increase in temperature at the front surface of the membrane. The thermal diffusion length in the direction of the membrane thickness is proportional

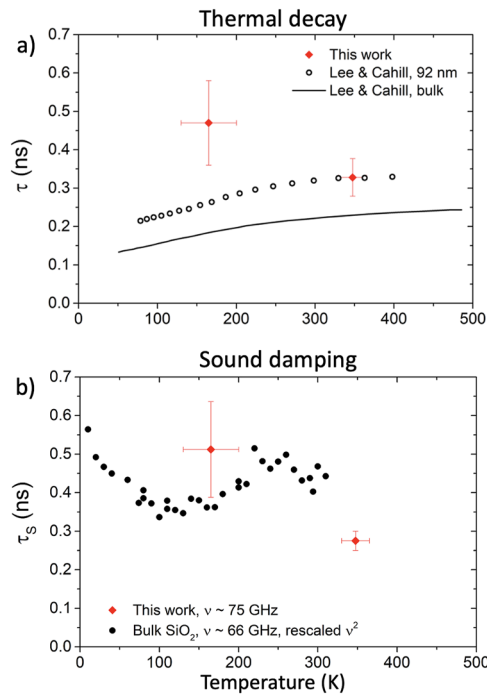


FIG. 5. Red diamonds in panel (a) are the decay of the thermal grating, parameter τ in Eq. (2), as a function of \bar{T} . Open circles are the values obtained by using the diffusivity for a SiO_2 film of 92 nm thickness deposited on a Si substrate by PECVD.³⁸ The black line is calculated using the diffusivity for a bulk sample of SiO_2 .³⁸ Panel (b) displays the attenuation of the LWs, parameter τ_s in Eq. (2), as a function of \bar{T} as red diamonds. Solid circles: sound attenuation of bulk SiO_2 measured by Brillouin ultraviolet spectroscopy at a frequency $\nu \sim 66$ GHz,¹⁵ rescaled assuming a quadratic frequency dependence. In both panels, error bars are obtained from the fitting routine.

to the square root of time and is given by the following expression: $L_{th}(t) = 2\sqrt{D_{th}t}$.⁴¹ Consequently, the temperature equilibrates all over the membrane volume in the time required for L_{th} to reach the membrane thickness as follows:

$$t = \frac{d^2}{4D_{th}} = \left(\frac{dq}{2}\right)^2 \tau = \pi^2 \left(\frac{d}{\Lambda_{TG}}\right)^2 \tau \approx 5 \text{ ns.} \quad (6)$$

In the present case, this value is an order of magnitude greater than τ so that the back side of the membrane is heated when the thermal grating has already decayed at its average temperature.

C. Sound attenuation

The attenuation of the Lamb waves, τ_s , is compared with data for the sound attenuation coefficient measured by means of UV Brillouin light scattering (UBLS) in bulk $\nu\text{-SiO}_2$ ¹⁵ in the lower panel of Fig. 5. The damping rate of the LWs is comparable to the thermal decay time, as indicated in Table I. UBLS¹⁵ on bulk $\nu\text{-SiO}_2$ measures the FWHM of the Brillouin peaks, Γ , while τ_s in Eq. (2) is the decay time of the amplitude of the wave; if Γ is measured in units of the angular frequency (rad/s), then $\tau_s = 2/\Gamma$. Reference 15 reports the internal friction, $Q^{-1} = \Gamma/\omega = 2/(\omega\tau_s) = 1/(\pi\nu\tau_s)$. The sound attenuation of vitreous silica in this temperature and frequency

range is known to follow an approximately quadratic frequency dependence.¹² For this reason, we have rescaled the τ_s derived from UBLS, multiplying those values by the square of the ratio between the average frequency of the two measurements, $\nu \approx 66$ GHz for UBLS and $\nu \approx 75$ GHz for EUV TG. For the latter value, we considered the average frequency of the two dominant Lamb waves (see Table II).

Panel (b) of Fig. 5 shows a qualitative agreement between the two datasets. In particular, our point at a higher temperature, the one with $T_i = 300$ K, suggests an increase in the anharmonic contribution to the sound damping as the temperature is increased above room temperature, in line with picosecond ultrasonic measurements.²⁰ The point at a lower temperature, $T_i = 50$ K, is slightly higher than expected. This discrepancy is probably related to the strong temperature inhomogeneity induced by the EUV TG excitation at low temperatures, where some regions of the membrane remain at 50 K, while others have an initial temperature of ~ 200 K. The TG waveform will probably do an average of the decay rates in this quite broad temperature interval so that the resulting τ_s is longer with respect to the value expected at \bar{T} , since at lower temperatures, the sound wave is expected to live longer.

V. CONCLUSIONS

We used EUV TG for studying the thermoelastic response of a 100 nm thick membrane of amorphous SiO_2 , a material that is transparent to the optical radiation most often used for this kind of studies. The use of EUV wavelengths in a TG experiment allowed us to explore the sub-100 nm wavelength range, without the need for nanostructuring or contact with the sample. In such a range, the characteristic timescale for heat transport is expected to become comparable to the lifetime of acoustic modes. Indeed, the observed thermoelastic response presents a relaxation of the thermal grating, occurring in the 300–500 ps timescale, roughly comparable to the expectations of Fourier law of diffusion, as well as modulations due to the propagation of Lamb modes, a kind of acoustic waveguide modes of mixed longitudinal–transverse character, which decay on a similar timescale. The ability of detecting the decay rate of transverse and longitudinal acoustic modes in disordered systems at sub-100 nm wavelength is essential for clarifying the mechanisms responsible for the thermal transport in amorphous solids.¹²

The same experiment was conducted by lowering the initial sample temperature to 50 K and keeping the EUV excitation intensity on a comparable level. An effect of temperature on the decay of acoustic modes is evident already on the raw data. A more detailed data analysis showed a non-constant (i.e., time-dependent) acoustic frequency in the EUV TG signal, which we interpret as a subtle temperature effect related to time-dependent changes in the temperature distribution, around an effective sample temperature determined by the total energy deposited into the sample by the FEL pulse. This effect likely arises from the inhomogeneity in the initial thermal distribution, due to the fact that the absorption length of the EUV excitation was shorter than the sample thickness. The comparison of the thermal and acoustic decay times extracted from the present experiment with literature values shows a substantial agreement when an average effective temperature is used. Time-dependent changes in the acoustic frequency were not observed when the sample was at

room temperature, and the estimated increase in the effective sample temperature was substantially lower, likely indicating how the amplitude of the temperature distribution is not sufficiently large for being appreciated. On the one hand, these results indicate how the EUV intensity at the sample should be lowered in low-temperature experiments for compensating the decrease in the value of the specific heat and avoiding time-dependent effects due to large thermal gradients. On the other hand, the use of large excitation intensities may allow us to follow the thermalization of the thermoelastic dynamics in the sub-ns timescale, which, in a broader context, can be of interest for non-equilibrium studies.

The EUV TG approach can be pushed to shorter wavelengths, potentially allowing the study of the thermal decay and of the sound propagation and damping in a wide frequency interval, up to frequencies approaching 500 GHz. Sound attenuation in the frequency interval between 100 GHz and 1 THz is responsible for the peculiar temperature dependence of the thermal conductivity of amorphous solids.¹² This frequency range is experimentally challenging, and the first results in a wide frequency interval on vitreous silica have appeared only very recently.²¹ Those results were obtained with the picosecond ultrasonic technique and can be used only on thin films of specific thickness covered with the appropriate transducer. The EUV TG method complements these approaches, allowing one to probe the thermoelastic properties of unsupported membranes. This technique can also be used to probe the surface acoustic waves in bulk samples in the same broad frequency range.⁸

ACKNOWLEDGMENTS

The authors would like to thank J. Roussie of SiMPore for the detailed information on the SiO₂ membrane preparation and physical properties. G. M. and A. M. acknowledge the support by the project BIRD-2021 from the University of Padova (I). The contribution by R.A.D., A.A.M., and K.A.N. was supported by the US Department of Energy, Office of Science, Office of Basic Energy Sciences, under Award No. DE-SC0019126. F.C. is a chargé de recherche of the Fonds de la Recherche Scientifique-FNRS.

AUTHOR DECLARATIONS

Conflict of Interest

The authors have no conflicts to disclose.

Author Contributions

Danny Fainozzi: Conceptualization (equal); Data curation (equal); Formal analysis (equal); Investigation (equal); Writing – original draft (equal). **Federico Caporaletti:** Investigation (equal). **Flavio Capotondi:** Investigation (equal); Writing – review & editing (supporting). **Dario De Angelis:** Investigation (equal). **Ryan A. Duncan:** Investigation (equal). **Laura Foglia:** Investigation (equal). **Alessandro Martinelli:** Investigation (equal); Writing – review & editing (supporting). **Riccardo Mincigrucci:** Data curation (supporting); Investigation (equal). **Keith A. Nelson:** Conceptualization (equal); Supervision (supporting). **Emanuele Pedersoli:** Investigation (equal). **Marco Zanatta:** Investigation (equal). **Alexei A.**

Maznev: Conceptualization (equal); Data curation (supporting); Formal analysis (supporting); Supervision (equal); Writing – review & editing (supporting). **Giulio Monaco:** Conceptualization (equal); Formal analysis (supporting); Investigation (equal); Writing – review & editing (supporting). **Filippo Bencivenga:** Conceptualization (equal); Data curation (equal); Formal analysis (equal); Investigation (equal); Writing – review & editing (equal). **Giacomo Baldi:** Conceptualization (equal); Data curation (equal); Formal analysis (equal); Investigation (equal); Writing – review & editing (equal).

DATA AVAILABILITY

The data that support the findings of this study are available from the corresponding author upon reasonable request.

REFERENCES

- X. Qian, J. Zhou, and G. Chen, “Phonon-engineered extreme thermal conductivity materials,” *Nat. Mater.* **20**, 1188 (2021).
- T. Rausch, E. Gage, and J. Dykes, in *Ultrafast Magnetism I: Proceedings of the International Conference UMC 2013 Strasbourg, France, October 28th–November 1st, 2013* (Springer, 2014), pp. 200–202.
- T. D. Frazer, J. L. Knobloch, J. N. Hernández-Charpak, K. M. Hoogeboom-Pot, D. Nardi, S. Yazdi, W. Chao, E. H. Anderson, M. K. Tripp, S. W. King *et al.*, *Phys. Rev. Mater.* **4**, 073603 (2020).
- D. G. Cahill, W. K. Ford, K. E. Goodson, G. D. Mahan, A. Majumdar, H. J. Maris, R. Merlin, and S. R. Phillpot, *J. Appl. Phys.* **93**, 793 (2003).
- F. Bencivenga and C. Masciovecchio, *Nucl. Instrum. Methods Phys. Res., Sect. A* **606**, 785 (2009).
- F. Bencivenga, R. Mincigrucci, F. Capotondi, L. Foglia, D. Naumenko, A. A. Maznev, E. Pedersoli, A. Simoncig, F. Caporaletti, V. Chiloyan *et al.*, *Sci. Adv.* **5**, eaaw5805 (2019).
- D. Naumenko, R. Mincigrucci, M. Altissimo, L. Foglia, A. Gessini, G. Kurdi, I. Nikolov, E. Pedersoli, E. Principi, A. Simoncig *et al.*, *ACS Appl. Nano Mater.* **2**, 5132 (2019).
- L. Foglia, R. Mincigrucci, A. A. Maznev, G. Baldi, F. Capotondi, F. Caporaletti, R. Comin, D. De Angelis, R. Duncan, D. Fainozzi *et al.*, *Photoacoustics* **29**, 100453 (2023).
- A. Milloch, R. Mincigrucci, F. Capotondi, D. De Angelis, L. Foglia, G. Kurdi, D. Naumenko, E. Pedersoli, J. S. Pelli-Cresi, A. Simoncig *et al.*, *ACS Appl. Nano Mater.* **4**, 10519 (2021).
- T. Metcalf, X. Liu, and M. R. Abernathy, *Mater. Res.* **21**, e20170863 (2018).
- M. Granata, A. Amato, L. Balzarini, M. Canepa, J. Degallaix, D. Forest, V. Dolique, L. Mereni, C. Michel, L. Pinar, B. Sassolas, J. Teillon, and G. Cagnoli, *Classical Quantum Gravity* **37**, 095004 (2020).
- G. Baldi, A. Fontana, and G. Monaco, *Low-Temperature Thermal and Vibrational Properties of Disordered Solids: A Half-Century of Universal “Anomalies” of Glasses* (World Scientific, 2022), pp. 177–226.
- P. Benassi, S. Caponi, R. Eramo, A. Fontana, A. Giugni, M. Nardone, M. Sampoli, and G. Vilianni, *Phys. Rev. B* **71**, 172201 (2005).
- C. Masciovecchio, G. Baldi, S. Caponi, L. Comez, S. Di Fonzo, D. Fioretto, A. Fontana, A. Gessini, S. C. Santucci, F. Sette, G. Vilianni, P. Vilmercati, and G. Ruocco, *Phys. Rev. Lett.* **97**, 035501 (2006).
- G. Baldi, S. Caponi, A. Fontana, P. Benassi, A. Giugni, M. Nardone, and M. Sampoli, *Philos. Mag.* **87**, 603 (2007).
- G. Baldi, V. M. Giordano, G. Monaco, and B. Ruta, *Phys. Rev. Lett.* **104**, 195501 (2010).
- G. Baldi, V. M. Giordano, and G. Monaco, *Phys. Rev. B* **83**, 174203 (2011).
- S. Ayrinhac, M. Foret, A. Devos, B. Rufflé, E. Courtens, and R. Vacher, *Phys. Rev. B* **83**, 014204 (2011).
- C. Klieber, E. Peronne, K. Katayama, J. Choi, M. Yamaguchi, T. Pezeril, and K. A. Nelson, *Appl. Phys. Lett.* **98**, 211908 (2011).

- ²⁰A. Huynh, E. Péronne, C. Gingreau, X. Lafosse, A. Lemaître, B. Perrin, R. Vacher, B. Rufflé, and M. Foret, *Phys. Rev. B* **96**, 174206 (2017).
- ²¹P. J. Wang, A. Huynh, T. C. Hung, J. K. Sheu, X. Lafosse, A. Lemaître, B. Perrin, B. Rufflé, R. Vacher, C. K. Sun, and M. Foret, "Quartic scaling of sound attenuation with frequency in vitreous silica," [arXiv:2310.11832](https://arxiv.org/abs/2310.11832) [cond-mat.mes-hall] (2023).
- ²²R. Vacher and J. Pelous, *Phys. Rev. B* **14**, 823 (1976).
- ²³C. Masciovecchio, A. Gessini, S. Di Fonzo, L. Comez, S. C. Santucci, and D. Fioretto, *Phys. Rev. Lett.* **92**, 247401 (2004).
- ²⁴R. Mincigrucci, L. Foglia, D. Naumenko, E. Pedersoli, A. Simoncig, R. Cucini, A. Gessini, M. Kiskinova, G. Kurdi, N. Mahne *et al.*, *Nucl. Instrum. Methods Phys. Res., Sect. A* **907**, 132 (2018).
- ²⁵F. Bencivenga, F. Capotondi, L. Foglia, R. Mincigrucci, and C. Masciovecchio, *Adv. Phys.: X* **8**, 2220363 (2023).
- ²⁶R. N. Carter, S. M. Casillo, A. R. Mazzocchi, J.-P. S. DesOrmeaux, J. A. Roussie, and T. R. Gaborski, *Biofabrication* **9**, 015019 (2017).
- ²⁷G. Carlotti, L. Doucet, and M. Dupeux, "Elastic properties of silicon dioxide films deposited by chemical vapour deposition from tetraethylorthosilicate," *Thin Solid Films* **296**, 102 (1997).
- ²⁸A. A. Maznev, R. Mincigrucci, F. Bencivenga, V. Unikandanunni, F. Capotondi, G. Chen, Z. Ding, R. Duncan, L. Foglia, M. Izzo *et al.*, *Appl. Phys. Lett.* **119**, 044102 (2021).
- ²⁹B. A. Auld, *Acoustic Fields and Waves in Solids* (Krieger Publishing Co., 1990).
- ³⁰J. S. Meth, C. D. Marshall, and M. D. Fayer, *J. Appl. Phys.* **67**, 3362 (1990).
- ³¹J. A. Rogers, A. A. Maznev, M. J. Banet, and K. A. Nelson, *Annu. Rev. Mater. Sci.* **30**, 117 (2000).
- ³²C.-S. Zha, R. J. Hemley, H.-k. Mao, T. S. Duffy, and C. Meade, *Phys. Rev. B* **50**, 13105 (1994).
- ³³H. McSkimin, *J. Appl. Phys.* **24**, 988 (1953).
- ³⁴H. McSkimin, *J. Acoust. Soc. Am.* **31**, 287 (1959).
- ³⁵A. Polian, D. Vo-Thanh, and P. Richet, *Europhys. Lett.* **57**, 375 (2002).
- ³⁶J. R. Rouxel, D. Fainozzi, R. Mankowsky, B. Rösner, G. Seniutinas, R. Mincigrucci, S. Catalini, L. Foglia, R. Cucini, F. Döring *et al.*, *Nat. Photonics* **15**, 499 (2021).
- ³⁷H. J. Eichler, P. Günter, and D. W. Pohl, *Laser-Induced Dynamic Gratings* (Springer-Verlag, 1986).
- ³⁸S.-M. Lee and D. G. Cahill, *J. Appl. Phys.* **81**, 2590 (1997).
- ³⁹R. C. Zeller and R. O. Pohl, *Phys. Rev. B* **4**, 2029 (1971).
- ⁴⁰J. J. Freeman and A. C. Anderson, *Phys. Rev. B* **34**, 5684 (1986).
- ⁴¹L. D. Landau and E. M. Lifshitz, *Fluid Mechanics* (Butterworth-Heinemann, 1987).